CHAPTER 9

SEISMIC LATERAL EARTH PRESSURES FOR RETAINING WALL BACKFILLED WITH UNSATURATED SOIL UNDER TRANSIENT FLOW

9.1 INTRODUCTION AND REVIEW OF EXISTING STUDIES

The previous chapter determined the seismic lateral earth pressures that occur in retained unsaturated backfills under the steady state flow condition. However, the flows within the unsaturated backfills are often time-dependent. The rainfall-induced infiltration significantly influences the transient flow within the variably saturated soil. A few analytical (Yeh 1989; Srivastava and Yeh 1991; Lu and Likos 2004; Lu and Godt 2013; Shahrokhabadi et al. 2019) and numerical (Zhang et al. 2016; Vahedifard et al. 2017; Yang et al. 2019) works are recently conducted to measure the spatially and temporally-dependent lateral earth pressure on unsaturated soil backfills. Nevertheless, these earth pressure estimations were performed under static conditions. No literature seems available for assessing the lateral earth pressure on unsaturated soil backfill under transient flow subjected to seismic loading. An attempt has been initiated in the present chapter to estimate the lateral earth pressure on homogeneous unsaturated soil backfill under transient infiltration subjected to horizontal and vertical seismic forces.

A series of analyses, comprising the active and passive state of failure, are conducted by duly modifying the Rankine’s classical earth pressure theory. The seismic forces are realized by considering the pseudo-static analysis. The transient flow is modelled with the usage of Richard’s one-dimensional nonlinear parabolic partial differential equation. The transient flow restricts the formation of the closed-form expression of suction stress above the water table. Hence, a numerical finite difference scheme is used to estimate the variation of suction stress with respect to time and space. A thorough investigation is carried out to understand the influences of the transient flow and seismic forces on the (a) earth pressure profiles, (b) failure (corresponding) surfaces, and (c) developed cracks (tensile).

9.2 PROBLEM STATEMENT AND CONSIDERED ASSUMPTIONS

A vertical retaining wall of height, H, as shown in Fig. 9.1, retains the homogeneous, isotropic, and cohesive-frictional soil in a half-space domain. Conventionally, retaining walls are plane-strain in nature. The backfill ground surface (GS) is horizontal, flat, and stress-free. It is to be noted that when the wall is vertical, and the retained ground surface is horizontal, the principal planes at any point are the horizontal and vertical planes. The soil-wall interface friction angle is considered to be zero. The retained backfill is subjected to seismic forces. The groundwater table (GWT) is located at the toe of the wall. The soil above and below the water table is assumed to remain in partially- and fully-saturated conditions, respectively. The fluid flow in the vadose zone is unidirectional (vertical), transient, and governed by Darcy's linear flow law. The variation of permeability and the volumetric water content (or degree of saturation) with respect to matric suction is assumed to be governed by Gardner's soil-water-characteristics curve (Gd-SWCC) and Gardner's one-parameter-dependent hydraulic conductivity function (Gd-HCF) (Section 6.2.1), respectively. The failure of soils is assumed to be dictated by Modified Mohr-Coulomb (MMC) yield criterion (Section 6.2.1). The soil strength parameters as well as Gd-SWCC and Gd-HCF model parameters are idealized to be independent of the net normal stress.

Considering these geometrical configurations and hydromechanical models, it is intended to assess the impact of transient infiltration on the seismic lateral earth pressures for two failure states, namely, active and passive conditions. The depth of the

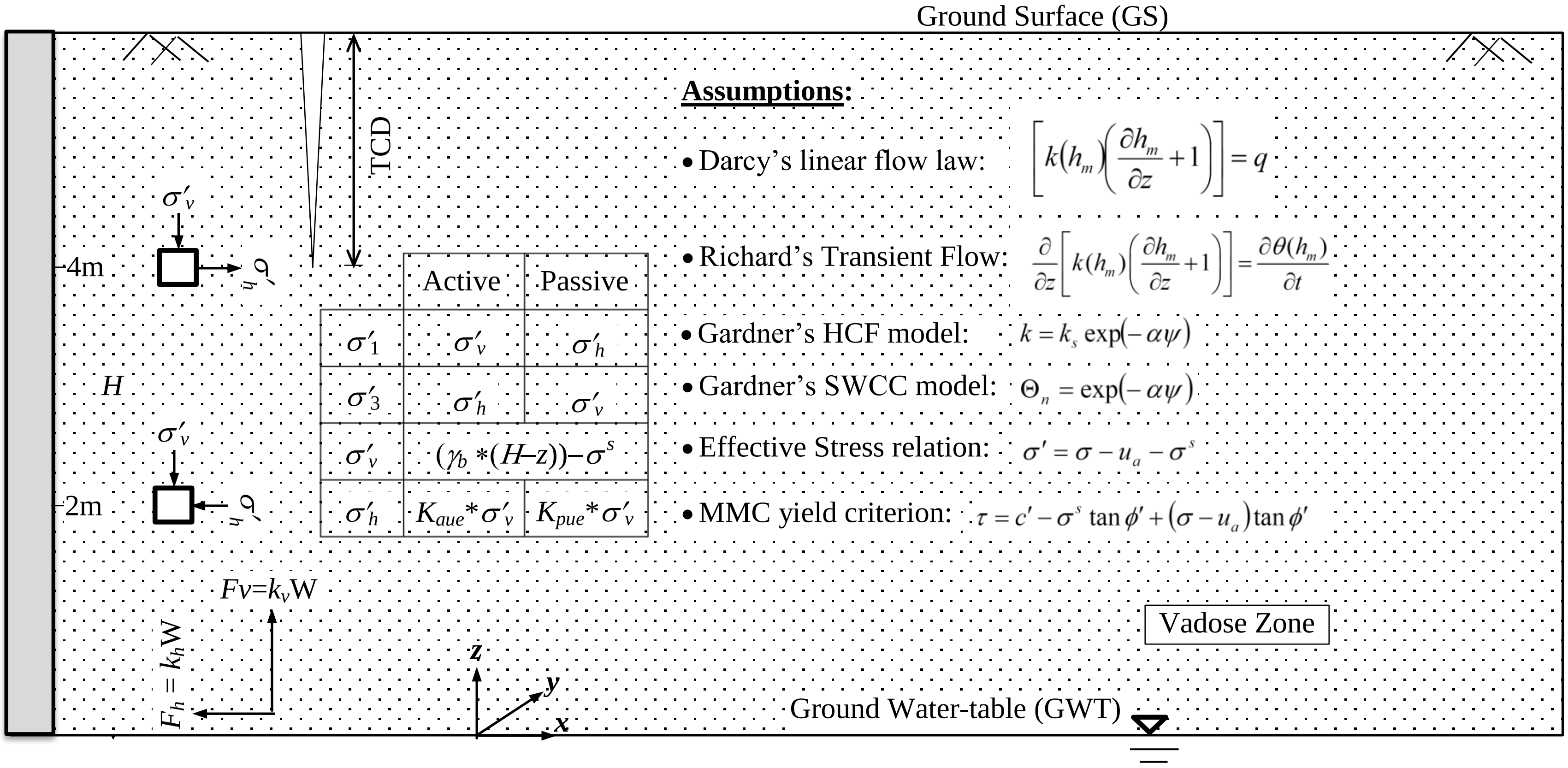

Fig. 9.1 Schematic diagram of the problem statement with the involved assumptions.

tensile crack developed during the active failure state is analytically estimated by assuming that the fluid pressure and the flow rate inside and outside the cracks are the same. A series of analyses are conducted to understand the combined effect of soil strength properties, hydraulic conductivity, SWCC model parameters, infiltration rates, and seismic loadings. The infiltration conditions are infused by considering the positive flow ratio, Q ($=q/k_s$). The extreme rainfall is realized by $Q=1$. The results are presented in terms of normalized values.

9.3 METHODOLOGY

9.3.1 Computation of lateral earth pressure

The following two-steps approach is adopted for computing the seismic lateral earth pressures in the unsaturated backfills under transient flows:

Step 1: Numerical (finite difference implicit scheme) estimation of the tempo-spatial variation of suction stress above the water table

Step 2: Analytical (limit equilibrium technique) evaluation of the lateral earth pressures, tension crack depths, and the failure surfaces with the obtained suction stress from Step-1.

9.3.2.1 Step 1: Computation of suction stress

The domain is first discretised with finite number of grid points as shown in Fig. 9.2. The quasi-implicit (Crank-Nicolson) discretised form of Richard’s transient equation (Eq. 6.13) is written explicitly for all the grids points. A simultaneous set of linear algebraic equations is written in compact matrix form, and thereafter, the boundary conditions are imposed adequately. Starting with the initial conditions, an iterative process is carried out to compute the matric suction head, and eventually, the spatially and temporal dependent suction stresses. The detailed procedure of suction

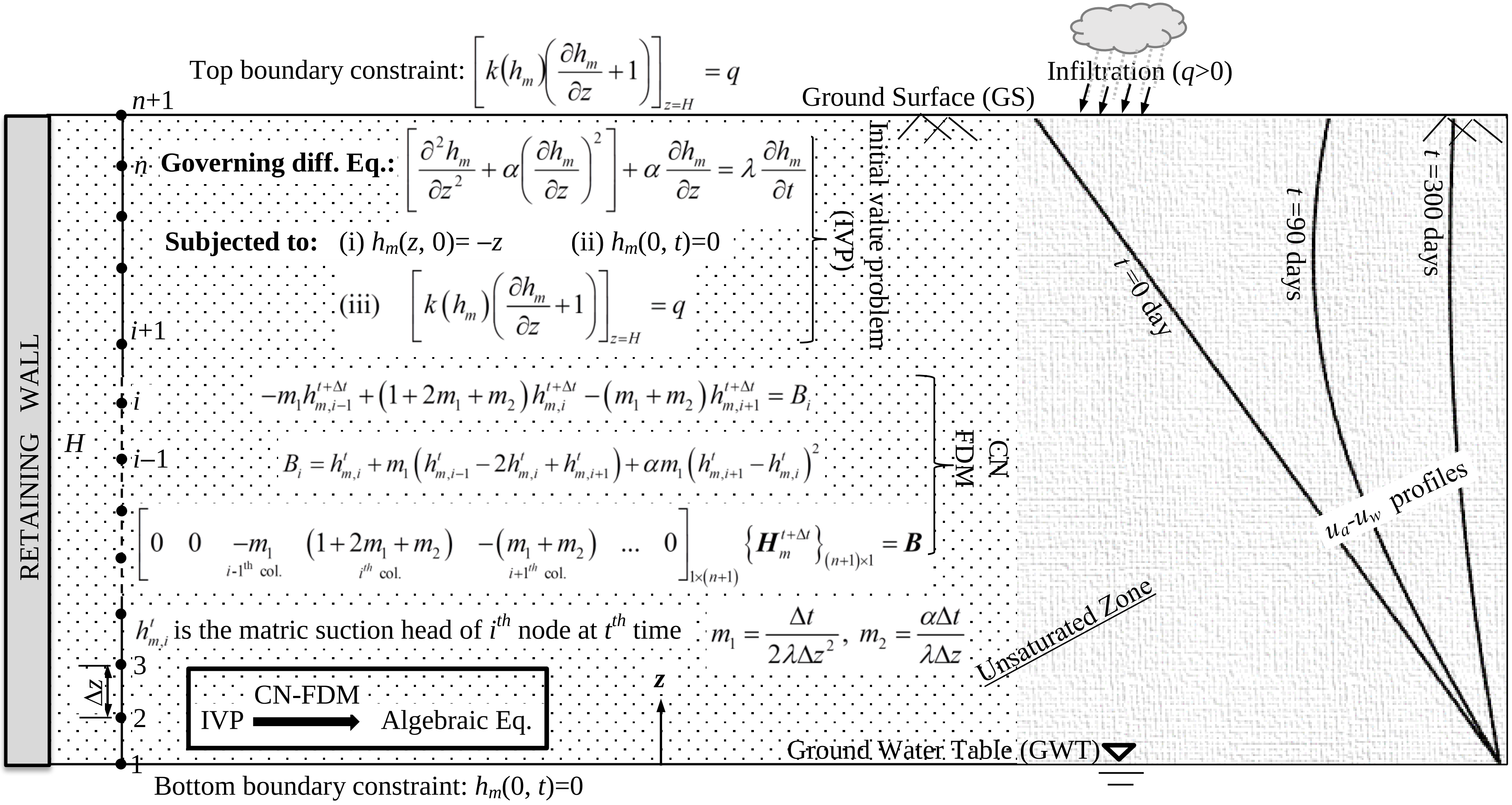

Fig. 9.2 Numerical scheme and the variation of matric suction with respect to time and space.

stress determination from transient flow analysis is elucidated in Section 6.2.3

9.3.1.2 Step 2: Computation of earth pressure under transient flow for seismic condition

The suction stress and, eventually, the effective stresses are evaluated using the vector $\boldsymbol{H_m}$ obtained in Step 1. Using the computed suction stress and following the work of a few researchers (Lu and Likos 2004; Jahangir et al. 2017), the seismic lateral earth pressures developed behind the retaining wall are assessed based on Rankine’s classical earth pressure theories. They are expressed below:

Active Earth Pressure (AEP): $\sigma_h' = K_{ae}\sigma_v' - 2c'\sqrt{K_{ae}} - 2\sigma^s\left(1 - K_{ae}\right)$ (9.1a)

Passive Earth Pressure (PEP): $\sigma_h' = K_{pe}\sigma_v' + 2c'\sqrt{K_{pe}} + 2\sigma^s(K_{pe} - 1)$ (9.1b)

here, the effective vertical (σ_v') and horizontal (σ_h') stresses are defined as:

$$\begin{Bmatrix} \sigma_v' \\ \sigma_h' \end{Bmatrix} = \begin{Bmatrix} \sigma_v - u_a - \sigma^s \\ \sigma_h - u_a - \sigma^s \end{Bmatrix} \tag{9.1c}$$

a) It is noteworthy that σ_v' and σ_h' are the major and minor principal stresses for the active failure; however, the sense of principal stresses is reversed during the passive failure. The three terms in Eqs. (9.1a) and (9.1b) represent the effect of self-weight, cohesive forces, and suction stresses, respectively. The existence of the last term reflects the presence of the variable saturation state of the soil. The inclusion of this suction-based term imparts the nonlinearity in the earth pressure profiles, which were otherwise linear for completely saturated soils. Irrespective of the failure states, the self-weight of the retained backfill always develops the compressive stresses; nevertheless, the second and the third terms exhibit either the tensional stress (active condition) or additional compressive stress (passive condition) based on the direction of wall movement.

b) Further, seismic force (F_h and F_v) induced- active (K_{ae}) and passive (K_{pe}) earth pressure coefficients of the retained backfills are adopted from the long-established and widely-used pseudo-static work of Mononobe and Okabe (1929):

$$K_{ae}, K_{pe} = \frac{\cos^2\left(\phi' - \eta\right)}{\cos^2\eta\left[1 \pm \sqrt{\dfrac{\sin\phi' \sin\left(\phi' - \eta\right)}{\cos\eta}}\right]^2} \tag{9.2}$$

$\phi' =$ Friction angle; $\eta = \tan^{-1}\left(\dfrac{k_h}{1-k_v}\right)$

$k_h =$ horizontal seismic coefficient = a_h / g

$k_v =$ vertical seismic coefficient = a_v / g

Seismic forces: $F_h = k_h W$ and $F_v = k_v W$;

W is the weight of the potential sliding mass

Note: (i) a_h and a_v are the seismic acceleration that creates inertial forces.

The earth pressure coefficients for the unsaturated soil subjected to the seismic loading can be expressed as under:

$$K_{aue} = \frac{\sigma_h - u_a}{\sigma_v - u_a} = K_{ae} - \frac{2c'\sqrt{K_{ae}}}{\sigma_v - u_a} - \frac{\sigma^s}{\sigma_v - u_a}\left(1 - K_{ae}\right) \tag{9.3a}$$

$$K_{pue} = \frac{\sigma_h - u_a}{\sigma_v - u_a} = K_{pe} + \frac{2c'\sqrt{K_{pe}}}{\sigma_v - u_a} + \frac{\sigma^s}{\sigma_v - u_a}\left(K_{pe} - 1\right) \tag{9.3b}$$

It is to be noted that K_{aue} and K_{pue} depend not only on the shear strength parameters (c', ϕ') but also on the suction stress and vertical overburden stress. Therefore, unlike the saturated soil backfill, the seismic earth pressure coefficients for the unsaturated soils vary spatially and thus result in the development of curvilinear earth pressure (total) profiles.

9.3.2 Computation of tension crack depth

The tensional stresses in the active failure state exhibit the development of the tensile crack in the unsaturated backfills. The existence of tension cracks induces a remarkable change in the computed earth pressure exerted on the retaining wall due to the reduction in slip surface and the weight of the cracked zone. The curtailment of the slip surface indicates that the mobilization of shear strength occurs along a relatively shorter length. The weight of the overburdened soil in the tension crack zone act as a surcharge on the top of the failure mass. As per Rankine’s earth pressure theory, the extent of the tensile crack from the ground surface is measured by equating the compressive and the tensional stresses, or, in other words, the net lateral stress at the crack tip is zero, i.e., $\sigma_h = \sigma_3 = 0$ (implying, $K_{aue} = 0$); this is also the portion where the complete tensile strength is mobilized. Hence, the tension crack depth (*TCD*) is expressed as:

$$TCD = \frac{2c'}{\gamma_b \sqrt{K_{ae}}} + \frac{\sigma^s}{\gamma_b}\left(1 - \frac{1}{K_{ae}}\right) \quad ; \quad \gamma_b \text{ is the bulk unit weight of the soil.} \qquad (9.4)$$

It is worth mentioning that, unlike the steady state, transient water flow does not produce any clear-cut explicit relation between σ^s and spatial positions. Hence, for determining the magnitude of *TCD*, the compressive and tensile stress profiles with respect to z are drawn in the first place. The intersection of these profiles provides the *TCD*. Fig. 9.3 shows such profiles corresponding to two different α’s (0.001 and 0.10) and after two different time periods, namely, t= 30 days and 90 days. Regardless of the unsaturated soil properties and the infiltration durations, the compressive stress profile will remain to be unique and linearly varying with depth; but the nonlinear tension stress profiles depend highly on the climatic condition, location of GWT, and the water retention capability of the soil. Therefore, the tensile crack depth not only varies with the soil's hydromechanical (i.e. strength, flow, SWCC, and HCF model parameters), and seismic properties but also on the elapsed time Due to the variation in suction stress, TCD extends in evaporation but closes during infiltration.

The numerical computations of the suction stress and the analytical evaluation of the AEP, PEP, and *TCD* are carried out by writing suitable code in MATLAB (version R2018a).

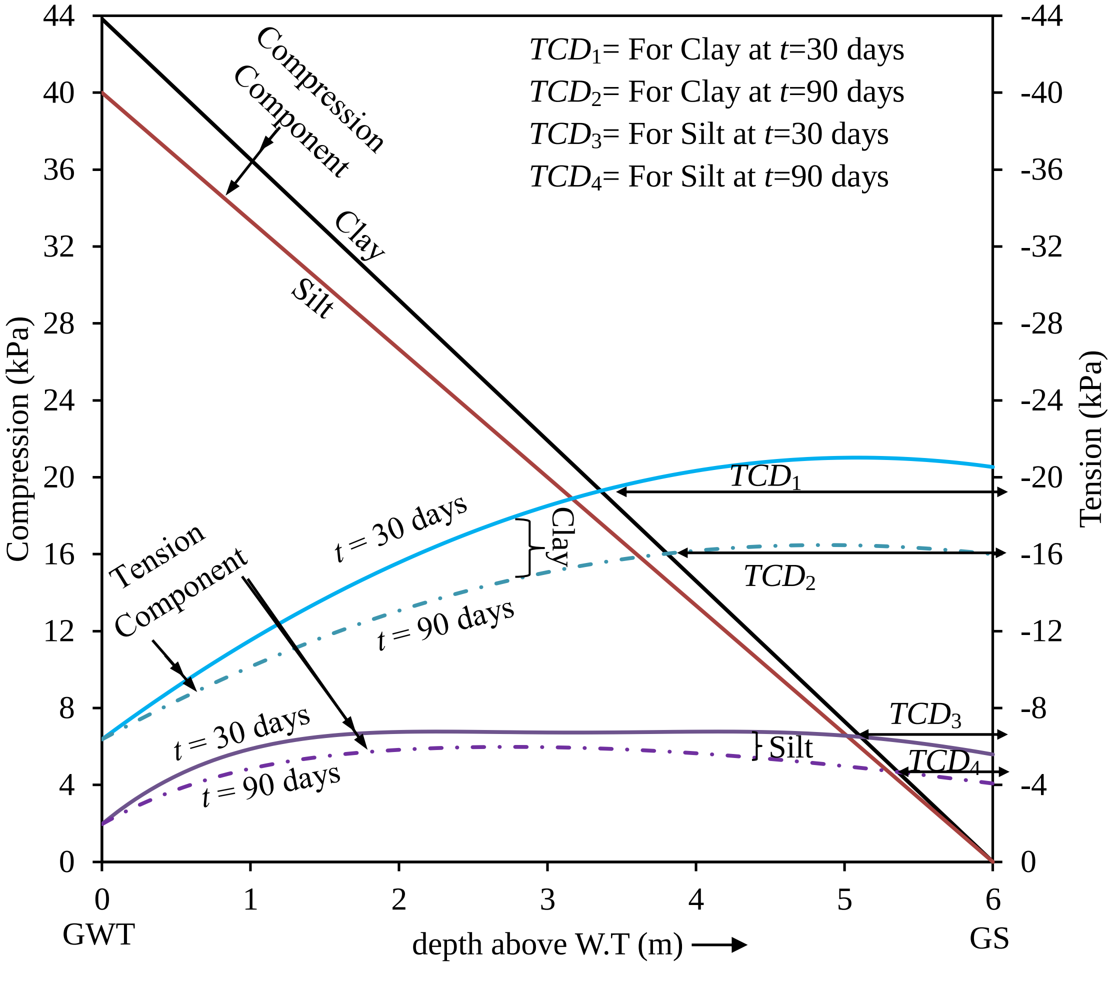

Note: *TCD* = Tension crack depth

Fig. 9.3 Crack depth determination by plotting the variation of tensile and compressive components of total active earth pressure above the water table.

9.4 FAILURE CIRCLES AND ENVELOPES

Irrespective of the saturation state, the application of dynamic load enhances the magnitude of K_{ae} but reduces K_{pe}; this eventually shows that the size of the Mohr's failure circle shrinks with the increase in seismicity. Fig. 9.4 presents the failure circles and the corresponding failure envelopes pertaining to static (k_h= k_v =0) and seismic (k_h= k_v =0.2) cases after different elapsed time, namely, t= 30 days and 300 days. With the advancement in time, the apparent cohesion at any point varies significantly due to the effect of suction stress; this results in parallel shifts of failure envelopes. However, due to the action of dynamic load, the soil shear strength and, consequently, the failure envelope no longer remain the same; the slope angle of the failure envelope or the maximum obliquity angle (shown as κ in Fig. 9.4) reduces. This reduction in strength is comparatively higher for the active condition than its passive counterpart. The variations of κ with η (which measures the seismic intensity and is expressed as $\tan^{-1}(k_h/(1-k_v))$, corresponding to various ϕ' values, are shown in Fig. 9.5. The profiles appear linear and parallel to each other up to a certain level of seismicity (η_c) shown by a pointed arrow. The higher the frictional strength higher would be the value of η_c.

9.5 PRESSURE PROFILES

To comprehend the combined effect of transient infiltration and seismicity on lateral earth pressures, a detailed parametric investigation is carried out on the three hypothetical soils of clay, silt, and fine sand. These soils' hydrological and mechanical properties are adopted from the previous literature (Lu and Likos 2004; Lu et al. 2010; Lu and Godt 2013; Shahrokhabadi et al. 2019) and presented in Table 9.1. The SWCC and the HCF profiles for the considered hypothetical soils are shown in Fig. 9.6. The height of the retaining wall is chosen to be 6m. Further, k_h is taken from 0 to 0.3 with

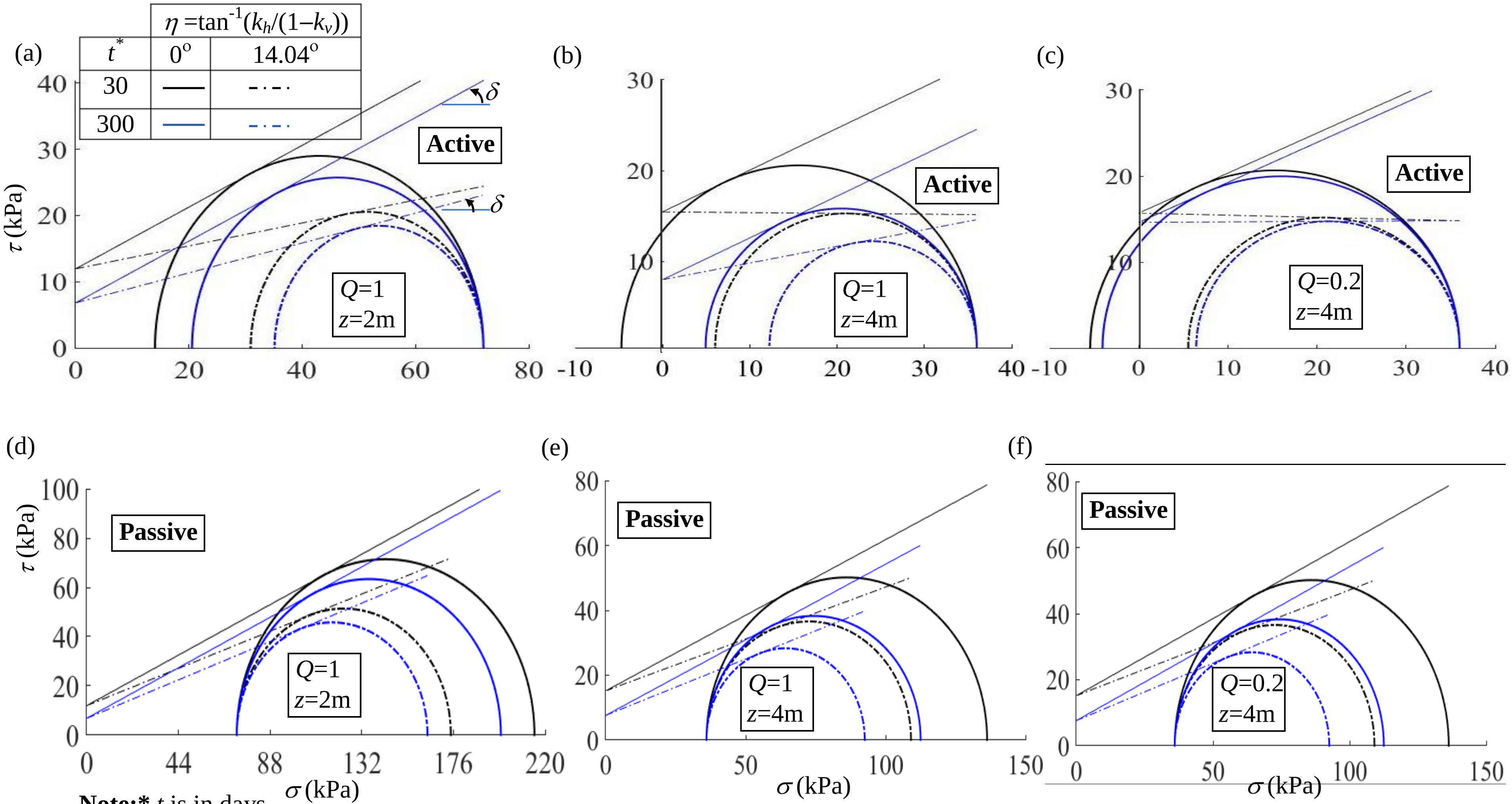

Note:* *t* is in days

Fig. 9.4 The size of the Mohr circles and the Mohr failure envelopes at two different duration and two different seismic levels (k_h=0, k_v=0 and k_h=0.2, k_v=0.2) corresponding to (a-c) active and (d-f) passive state and different combinations of Q and z: (a,d) Q =1, z=2; (b,e) Q =1, z=4; and (c,f) Q =0.2, z=4.

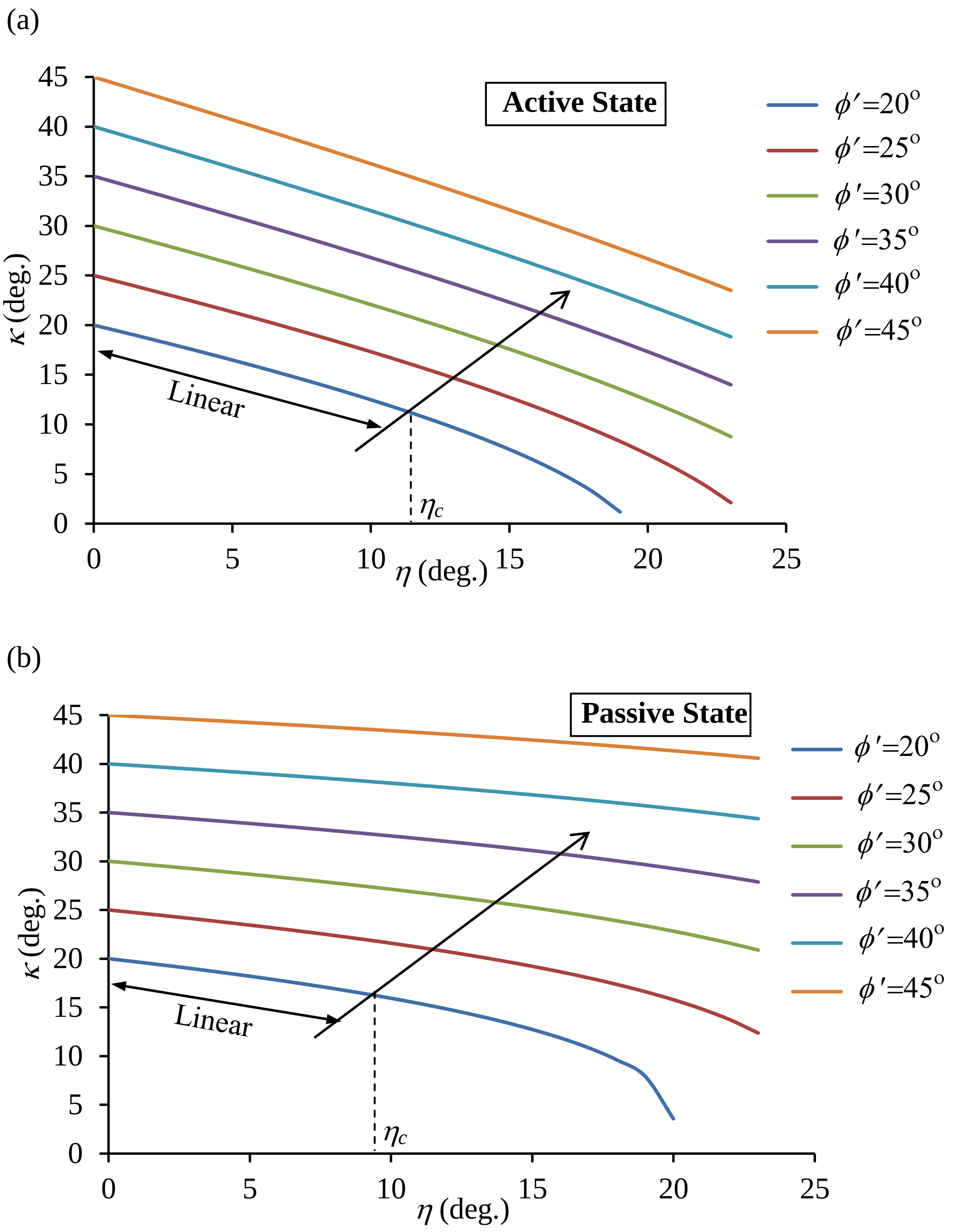

Note: $\eta = \tan^{-1}\left(\dfrac{k_h}{1-k_v}\right)$

Fig. 9.5 The variation of κ with respect to η for various ϕ' subjected to Q = 1**,** α =0.7m^{-1}, z=2m.

an interval of 0.1, and the k_v is chosen as 0, 0.5k_h, and k_h. The analyses are performed for three different infiltration rates: Q equals 0.2, 0.4, and 1.0; Q=1.0 indicates extreme infiltration due to heavy precipitation loading.

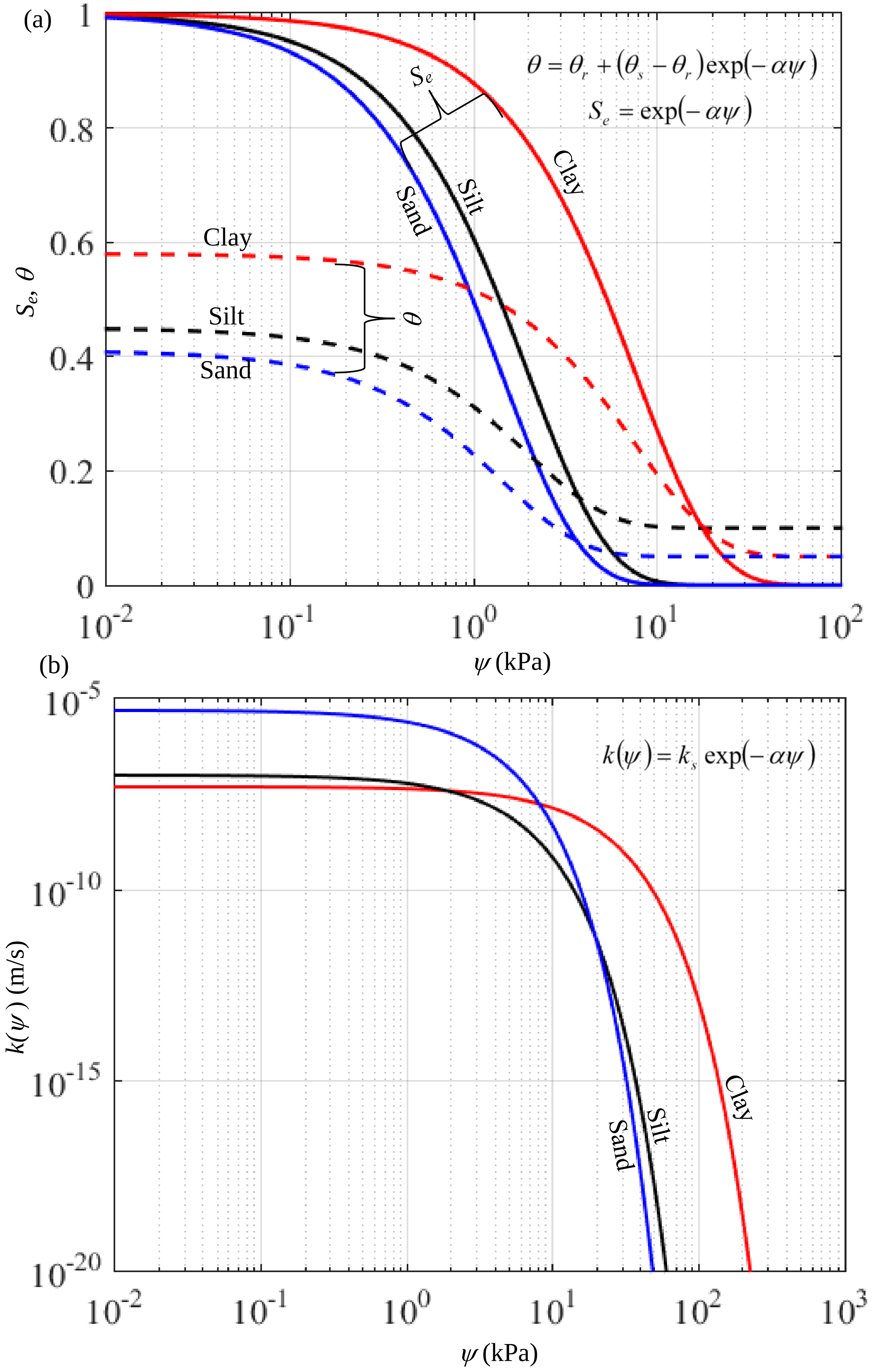

Fig. 9.6 The SWCC and the HCF profiles for the chosen hypothetical soils.

Table 9.1 The chosen hydro-mechanical properties from previous studies (Lu and Godt 2013; Shahrokhabadi et al. 2019).

Soil Type	α (m^{-1})	k_s (m/s)	θ_s	θ_r	c'(kPa)	ϕ' (deg.)	γ(kN/m^3)
Clay	0.13	5.0 x 10^{-8}	0.58	0.05	5	25	18
Silt	0.5	1.0 x 10^{-7}	0.45	0.10	1.7	30	20
Sand	0.7	5.0 x 10^{-6}	0.41	0.05	0.0	35	18

9.5.1 Pore-water pressure and suction stress profiles

Corresponding to the considered hypothetical soils, the variations of normalized matric suction (ψ_{norm}) and normalized suction stress (σ^s_{norm}) above the water table are plotted as a function of time and depicted in Fig. 9.7; the normalization is done with respect to the overburden pressure of the respective soil measured at the GWT ($\gamma_b H$). With time, the matric suction profiles invariably run from the inclined straight line (shown with the broken red line for t=0day) towards the vertical line (zero suction line). However, the σ^s_{norm} profiles drawn at different times lie on either side of the 0-day σ^s_{norm} profile. The tensile stresses for fine-grained soils are notably higher than their coarser counterpart. Moreover, the time required for attaining zero suction stress is considerably higher for clays (>450 days), followed by silts (around 300 days), and further followed by sand (<10 days). The shape of the ψ_{norm} and σ^s_{norm} profiles, especially for the coarse-grained soils, are distinct at the beginning of infiltration; however, with progress in time, the pattern of the ψ_{norm} and σ^s_{norm} profiles developed in the vadose zone are similar. Unlike clays, the profiles for sands manifest the existence of pronounced peak points at the vicinity of the GWT. It is also noted that the infiltration rate impacts ψ and/or σ^s contours at a higher duration. The transient impact

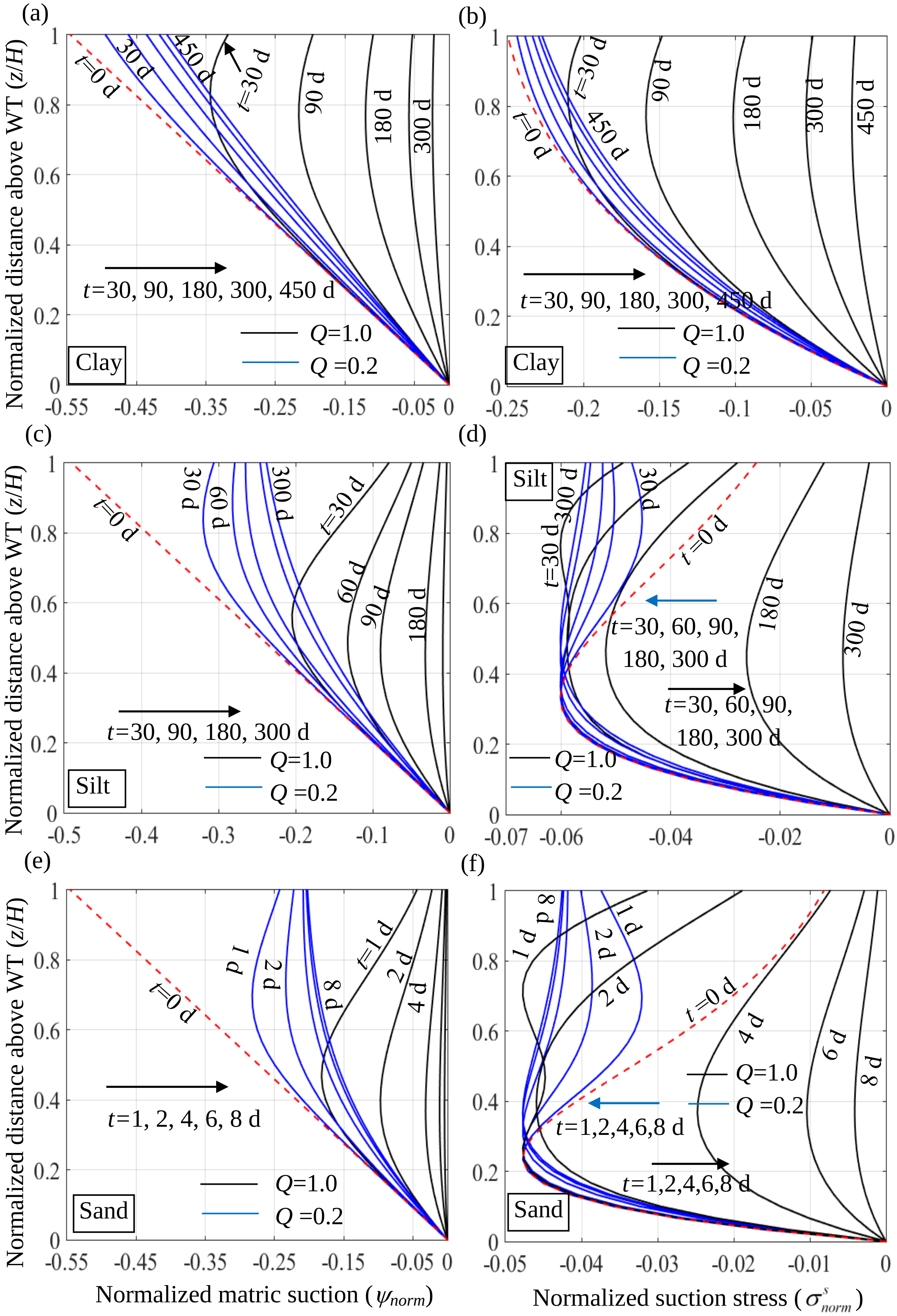

Fig. 9.7 The temporal variations of normalized (a, c, e) matric suction (ψ_{norm}) and (b, d, f) suction stress (σ^s_{norm}) above the water table for (a-b) clays, (c-d) silts, and (e-f) sands.

in the local scale is viewed by plotting the variation of the ψ_{norm} and σ^{s}_{norm} profiles at two different locations (i.e. z/H=0.6 and 0.8) subjected to two infiltration rates, namely, Q=0.2 and Q=1.0. Fig. 9.8 shows such variations for silty and sandy soils. The figure depicts that irrespective of the soil type and infiltration rate, the ψ_{norm} profile monotonically increases for both locations, whereas the trend of the σ^{s}_{norm} curves follow different patterns. Notably, the variation of matric suction and, eventually, the suction stress is not considered along the lateral extent; the spatial variation of suction occurs only along the depth (vertical scale) of the vadose zone. Consequently, the suction stress profiles both in close proximity to and at a considerable distance from the retaining wall exhibit identical characteristics.

The approximate solutions obtained from the present numerical scheme are further compared with the analytical values provided by Shahrokhabadi et al. (2019) based on the Laplace transformation. Fig. 9.9 presents such comparisons. The ψ_{norm} and σ^{s}_{norm} curves obtained from the present numerical technique and the reported analytical method match exactly for clays and provide a reasonably good agreement for sandy soils; nevertheless, a noticeable deviation is observed in silts. These discrepancies are insignificant near the GWT and are primarily viewed within the region between the GS and the peak point. However, these deviations diminish over time.

9.5.2 Earth pressure profiles for static conditions

Fig. 9.10 shows the variation of normalized AEP ($p_{active}/(\gamma_b H)$) and PEP ($p_{passive}/(\gamma_b H)$)) profiles in the vadose zone of the considered hypothetical soils under different infiltration rates without considering any seismic loading; Figs. 9.10 a, c, and e pertain to the normalized AEP, whereas Figs. 9.10 b, d, and f corresponds to normal-

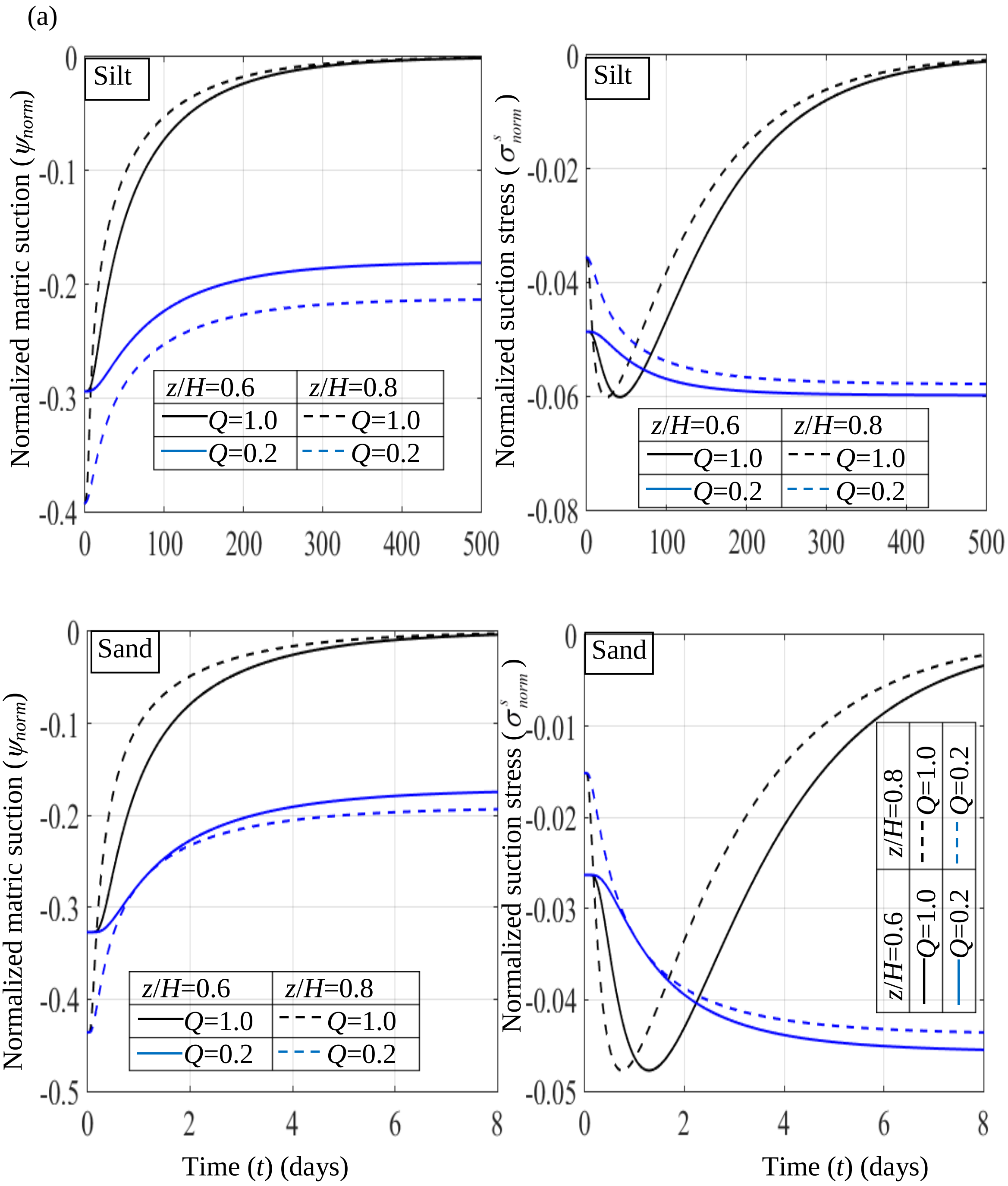

Fig. 9.8 Corresponding to two different spatial points and two flow ratios, the temporal variation of (a,c) σ^s_{norm} and (b,d) ψ_{norm} profiles for (a-b) silts, and (c-d) sands.

ized PEP. Due to the tensile component, the normalized p_{active} profiles near the ground surface stretch to the left (negative) side of the zero-earth pressure (as shown by the dashed vertical line) line. The spread of the normalized AEP at the ground surface is denoted by $AEP_{n,gs}$. The normalized $p_{passive}$ profiles always remain on the positive side.

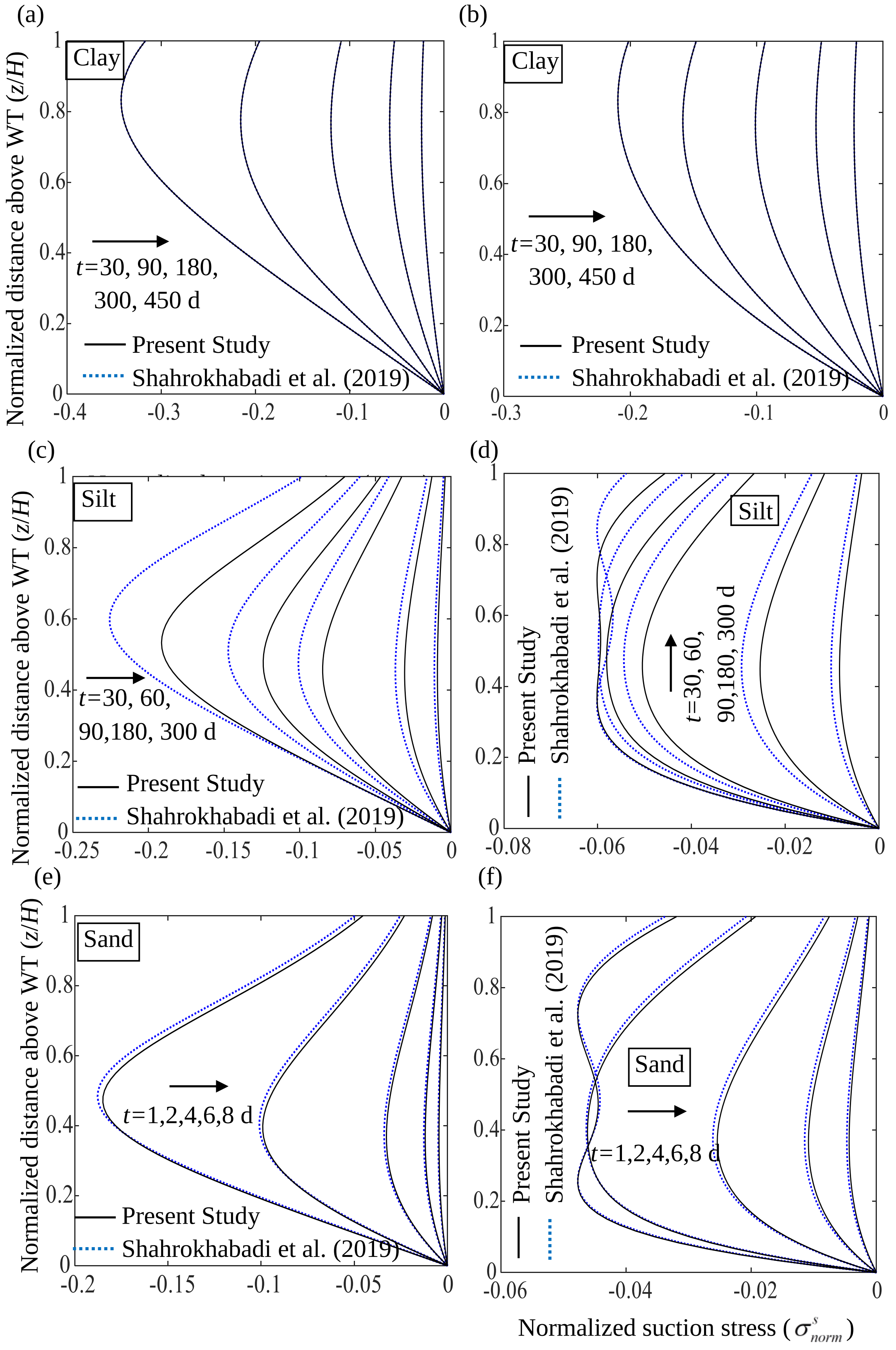

Fig. 9.9 Comparative study of σ^s_{norm} and ψ_{norm} profiles between the analytical solution of Shahrokhabadi et al. (2019) and numerical methods of the present study for (a, b) clay, (c, d) silt, and (e, f) sand.

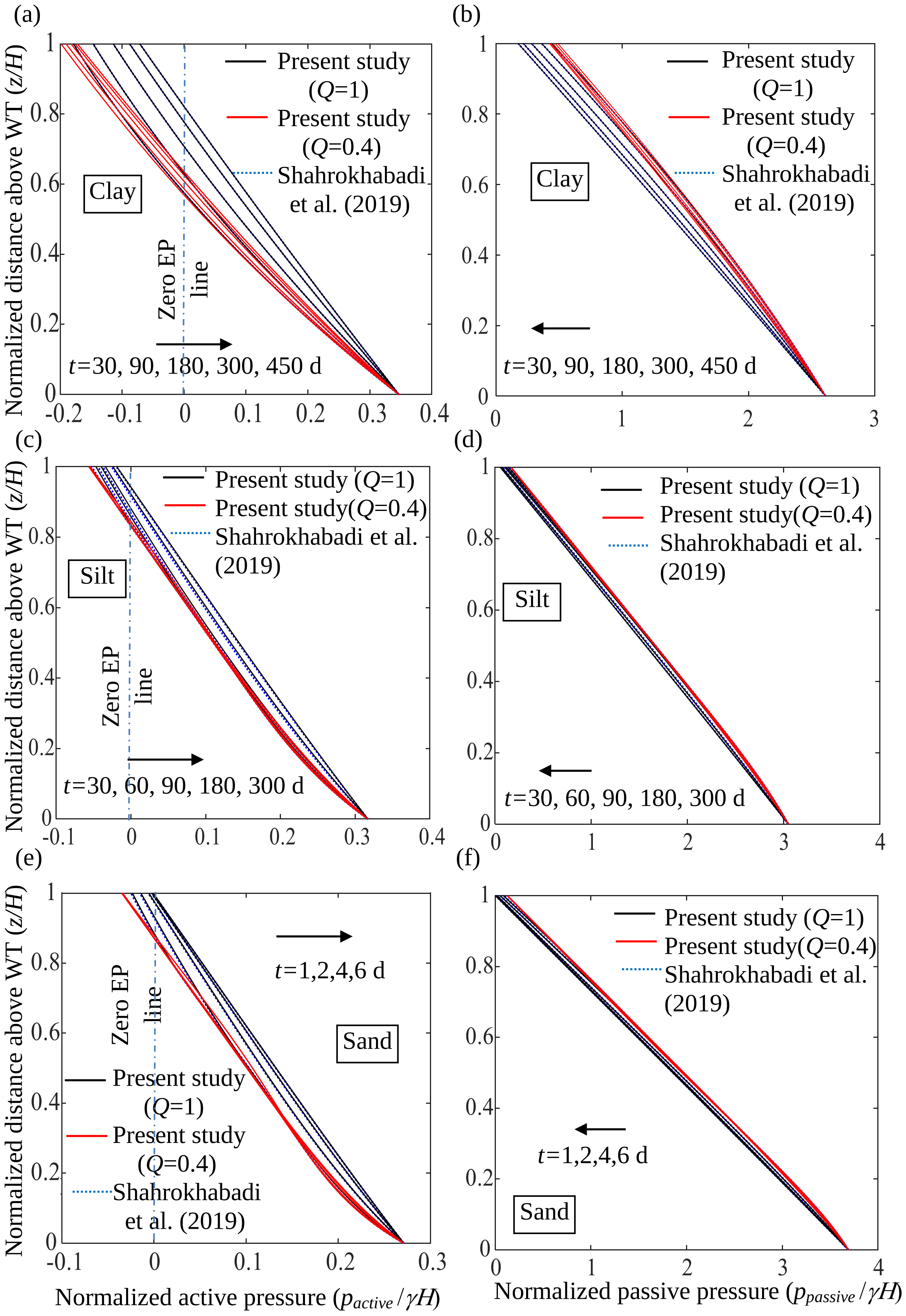

Fig. 9.10 Comparative study of normalized active and passive earth pressure between the analytical solution of Shahrokhabadi et al. (2019) and numerical methods of the present study for (a, b) clay, (c, d) silt, and (e, f) sand.

Irrespective of the soil type and the direction of the wall movement, the nonlinearity of the EP profiles decreases with the increase in the infiltration duration. The extent of the tensile zone from the ground surface further reduces with the increasing infiltration duration and intensity.

Figs. 9.10a and 9.10c demonstrate that corresponding to the extreme infiltration rate (Q=1), the tensile crack at t=30 days extends up to a depth of 0.42H and 0.15H for clay and silty backfills, respectively; however, for the same infiltration rate, the crack remains open up to a depth of 0.18H (clay) and 0.05H (silts) at t=450 days. Table 9.2 shows the computed TCD and $AEP_{n,gs}$ for the considered hypothetical soils. It is observed that with the increase in infiltration duration and intensity, the crack openings shrink and $AEP_{n,gs}$ reduces to a noticeable extent. The effect of infiltration duration is significant, especially for fine-grained soils subjected to a high infiltration rate (Q=1). For a moderate infiltration rate (Q=0.4), the closure of the crack openings and the reduction of the $AEP_{n,gs}$ take a very long time. The range of the tensile zone in sandy backfills is relatively small compared to its clay and silt counterpart. For the chosen sands, the tensile opening diminishes at t = 6 days when the infiltration rate is extreme (Q=1). However, for Q=0.4, the TCD and $AEP_{n,gs}$ values corresponding to t = 1 day and t = 6 days differ negligibly. The tensile cracks are the disconnected mass and do not exert any lateral pressure. Due to the discontinuity between the soil and the wall, the frictional strength and the suction stress are not considered in determining the active thrust acting on the retaining wall. Instead, the cracked zone contributes only to the surcharge loading over the lower wall height.

Fig. 9.10b depicts that with the passage of infiltration time, the normalized PEP in clays appreciably decreases for Q=1; however, for Q=0.4, the reduction of the PEP appears to occur at a prolonged rate. It can be summarized that with an increase in time,

Table 9.2 The computed values of *TCD* and $AEP_{n,gs}$ corresponding to various Q, t, and k_h.

			Q=1		Q=0.4		Q=0.2	
k_h	Soil type	t (days)	*TCD*	$AEP_{n,gs}$	TCD	$AEP_{n,gs}$	TCD	$AEP_{n,gs}$
0.0	Clay	30	0.42H	–0.18	0.43H	–0.20	–	–
		450	0.18H	–0.08	0.37H	–0.17	–	–
	Silt	30	0.15H	–0.05	0.17H	–0.07	–	–
		300	0.06H	–0.02	0.14H	–0.06	–	–
	Sand	1	0.12H	–0.02	0.14H	–0.03	–	–
		6	0.01H	–0.001	0.15H	–0.028	–	–
0.1	Clay	30	0.36H	–0.17	–	–	0.38H	–0.19
		450	0.14H	–0.06	–	–	0.36H	–0.18
	Silt	30	0.13H	–0.04	–	–	0.14H	–0.05
		300	0.04H	–0.01	–	–	0.13H	–0.04
	Sand	1	0.08H	–0.01	–	–	0.10H	–0.02
		8	0	0	–	–	0.08H	–0.018
0.3	Clay	30	0.19H	–0.12	–	–	0.21H	–0.17
		450	0.10H	–0.05	–	–	0.20H	–0.168
	Silt	30	0.04H	–0.02	–	–	0.08H	–0.04
		300	0.02H	–0.008	–	–	0.07H	–0.038
	Sand	1	0.03H	–0.007	–	–	0.03H	–0.02
		8	0	0	–	–	0.02H	–0.018

the total AEP increases, but the total PEP decreases. However, Figs. 9.10d and 9.10f depict that the transient effects are hardly prominent on normalized PEP profiles for silts and sands, even when the wetting phase is exceptionally rapid. The obtained solutions are further verified with the available solutions of Shahrokhabadi et al. (2019). A good agreement is observed between both the solutions.

9.5.3 Earth pressure profiles for seismic conditions

Fig. 9.11 depicts the seismic EP profiles above the water table for two different infiltration rates, namely, Q=0.2 and Q=1.0; Figs. 9.11a-9.11d represent the normalized pressure profiles for the active state, whereas Figs. 9.11e-9.11h denote the normalized PEP profiles. Two horizontal seismic forces are considered in this account, namely,

k_h=0.1 and k_h=0.3. Fig. 9.12 further presents the effect of vertical seismic load on the EP profiles. It is clearly observed that the presence of seismic forces decreases the tensile stress on the ground surface and substantially reduces the overall tensile crack zone. The effect of seismicity is more visible for the high infiltration rate. For a low infiltration rate, the effect of transient flow becomes utterly insignificant in the presence of seismic forces; nevertheless, for static loading, the variations in the AEP profiles are still visible even for the low percolation rate. It can be encapsulated that with the increase in dynamic loading, the effect of transient flow gets suppressed, and the nonlinearity of the EP profiles subsides. Further, the application of seismic acceleration impacts the AEP profiles more than the PEP profiles. Compared to horizontal acceleration, the impact of vertical acceleration on the transient flow is substantially limited.

9.6 CRACK DEPTH VARIATION

Fig. 9.13 presents the variation of the tensile crack depth with respect to the α parameter corresponding to (a) two infiltration durations (t=30 days and 90 days), (b) two flow rates (Q=0.2 and 1), and (c) three different sets of seismic loadings (η=0°, 11.31°, and 14.04°); where, $\eta=\tan^{-1}(k_h/(1-k_v))$. The seismic acceleration pertaining to η=0°, 11.31°, and 14.04° are (0.0,0.0), (0.2,0.0), and (0.2,0.2), respectively; the first and the second terms in the parenthesis represent k_h and k_v. The *TCD* decreases significantly with the increase in α value, infiltration duration, and/or seismic loadings. It is assumed that the immersed water within the tensile crack does not seep into the deeper soil and hence, the change in suction locally around the crack is conventionally ignored; however, the exerted pore water pressure along the tensile crack needs to be incorporated in the earth pressure calculation. The *TCD* profiles with

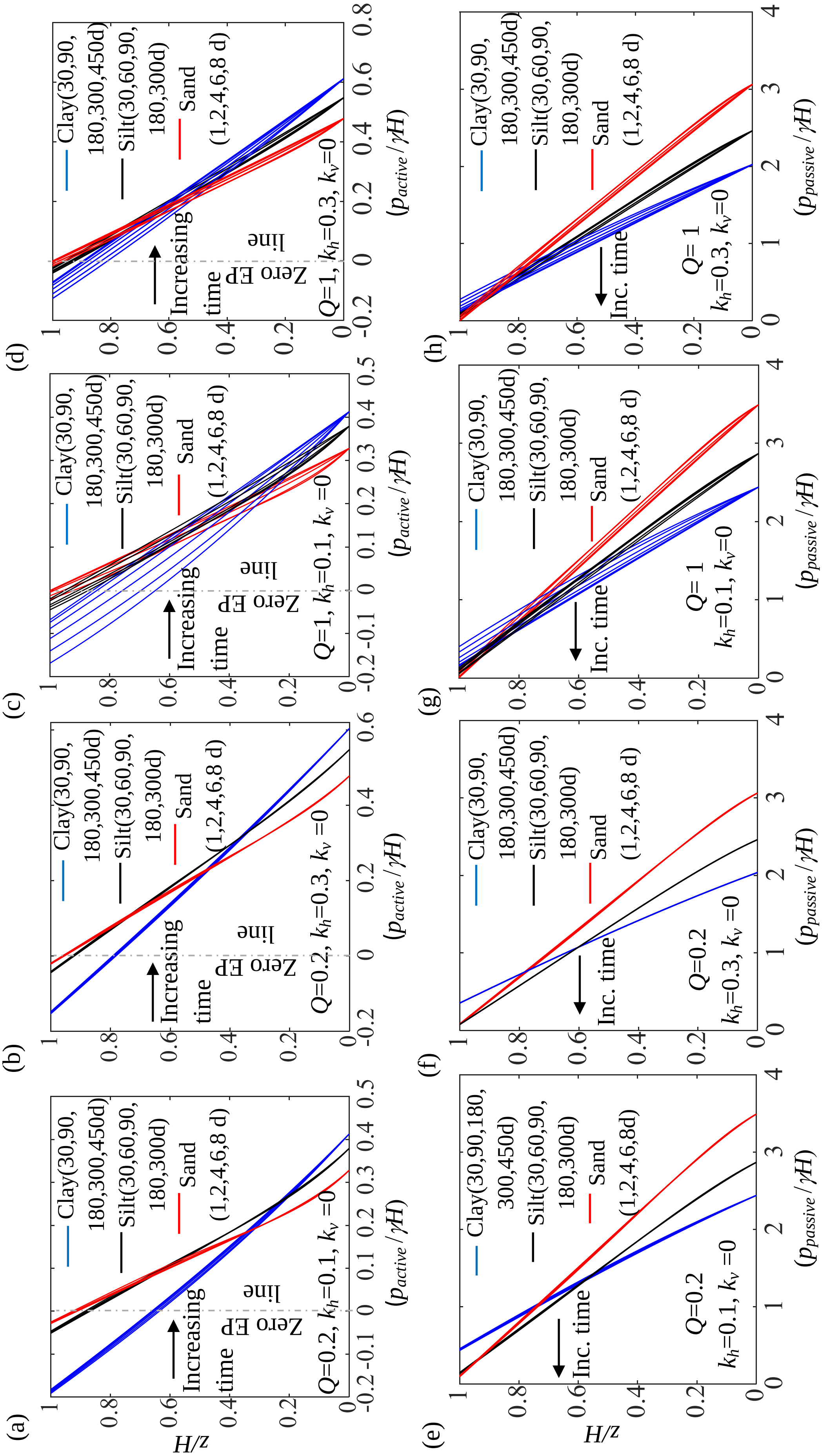

Fig. 9.11 The spatial variation of normalized (a-d) AEP and (e-h) PEP profiles corresponding to (a-b, e-f) Q=0.2 and (c-d, g-h) Q=1.0 with (a,c,e,g) k_h =0.1, and (b,d,f,h) k_h =0.3.

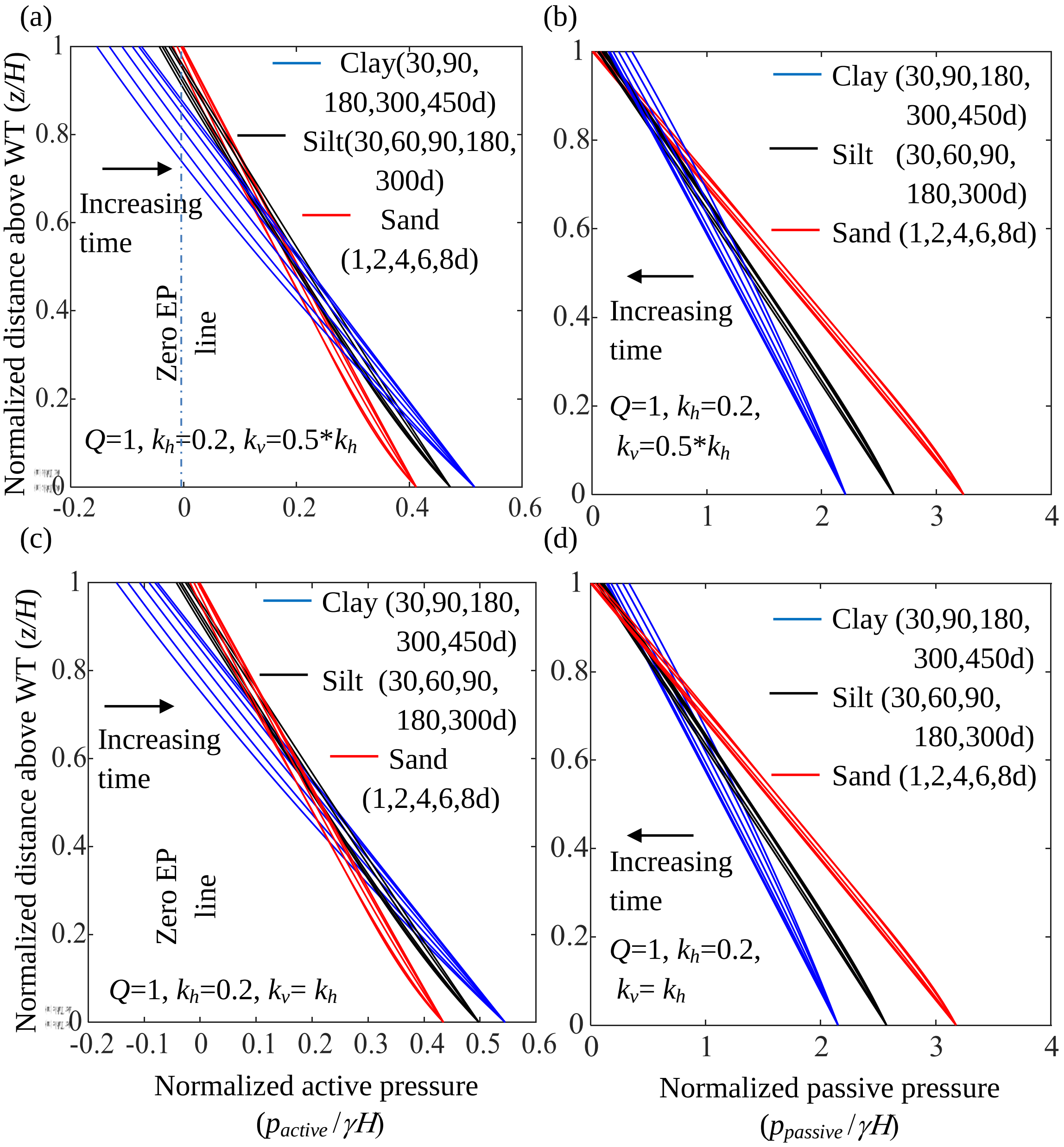

Fig. 9.12 The spatial variation of normalized (a-b) AEP and (c-d) PEP profiles subjected to Q=1, k_h = 0.2, and k_v equal to (a-b) 0.5 k_h and (b) k_h.

respect to α value appear to be highly nonlinear and upwardly convex; nevertheless, the decrement rate of *TCD* with increasing α appears to be faster for the low infiltration rate. Therefore, the crack openings are a bit larger for Q=1. Irrespective of the flow rate and the loading condition (static/ seismic), the *TCD* profiles corresponding to 30 days and 90 days appear to converge for low AEV soils. The crack depth ceases to exist for coarser soil.

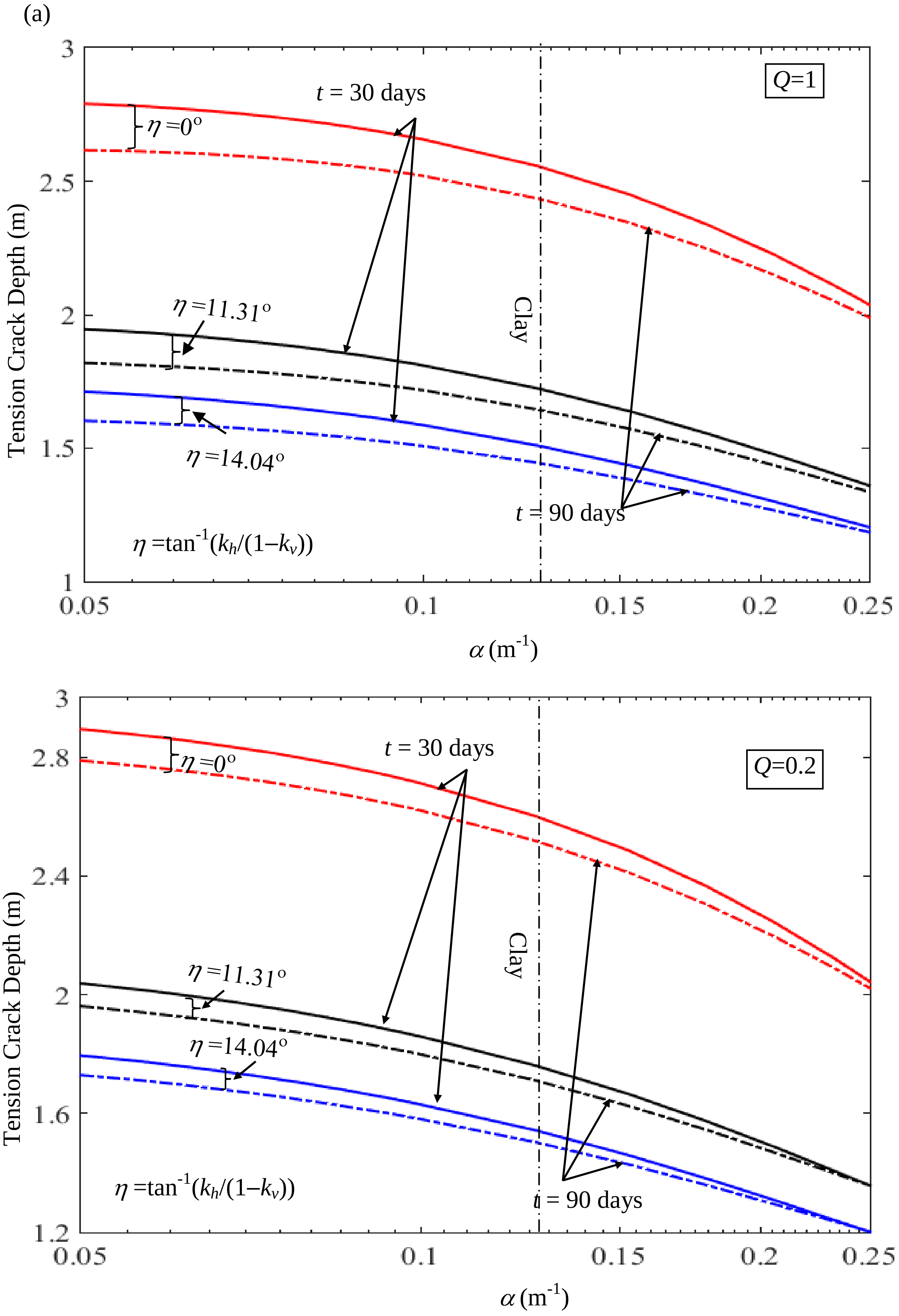

Fig. 9.13 The variation of TCD with respect to α corresponding to two different times (t = 30 and 90 days) and subjected to various η with (a) Q=1.0, (b) Q=0.2.

9.7 SUMMARY

The present chapter primarily investigates the effect of transient flow and seismic loadings on the active and passive earth pressures developed in retained unsaturated backfills. The seismic earth pressures are calculated by duly incorporating the variation of suction stress with space and time. A finite-difference solution for one-dimensional transient unsaturated flow is implemented into the suction-stress-based effective stress formulation. The analyses are carried out by suitably modifying Rankine's earth pressure theory and employing Richard's equation, Gardner's SWCC model, and Gardner's one-parameter HCF model. The effect of transient infiltration and the seismic loading on the Mohr failures circles, Mohr-Coulomb failure envelopes, pore water pressure profiles, suction stress profiles, earth pressure (active/ passive) profiles, and tension crack depths are extensively investigated and interpreted with insightful specificity.

9.8 LIMITATIONS

The present solution is not applicable to situations where the backfill has a significant slope. Moreover, the assumption of homogeneous and isotropic soil may not properly capture the complexities of actual soil conditions. Additionally, the soil-wall interface friction angle is considered to be zero. In reality, the existence of friction at the soil-wall interface can exert a substantial influence on lateral earth pressure. It is also considered that the groundwater table (GWT) is located at the toe of the wall. Variations in GWT may have a considerable effect on the lateral earth pressure. Furthermore, in the present study, the pseudo-static approach is utilized for the seismic analysis, omitting the precise consideration of inertial effects associated with dynamic loading. Design charts, accounting for specified parametric variations, are showcased to facilitate the determination of lateral earth pressures.